Chapter 10

Comparison of Additive Technologies for Gradient Aerospace Part Fabrication from Nickel-Based Superalloys

Igor V. Shishkovsky, Aleksey P. Nazarov, Dmitry V. Kotoban and Nina G. Kakovkina

Additional information is available at the end of the chapter

http://dx.doi.org/10.5772/61121

Abstract

In our papers, the laser beam-aided control of the self-propagating high-temperature synthesis in Ni–Al systems for the layerwise manufacture of three-dimensional (3D) parts was offered and experimentally realized. As for the laser in situ synthesis of NiAl and Ni_3Al intermetallides and their layerwise laser cladding without any visible cracks and pores, it was successfully performed later on. The present chapter is dedicated to the comparison of optimal conditions for the selective laser melting and laser direct metal deposition processes of the nickel-based powders and fabrication of a full-density, functionally graded, and crack-free structures on the maximum deposition rate for technological applications. The effects of laser parameters on the phase composition and microstructure of the resulting intermetallic samples will be discussed.

The possibility of controlling to change the hardness of the gradient structures from layer to layer by changing of the powder composition and by using the reinforced intermetallic inclusions into superalloy matrix widens the range of possible applications of 3D parts in aerospace and nuclear industries. Comparing different methods of additive manufacturing reveals their advantages and disadvantages for making large samples, scalability, and customizability, finding ways to control the distribu-

tion of residual stresses and specified grain-growth direction for the fabrication of more functional and high-precision samples.

Keywords: Selective laser melting (SLM), direct metal deposition (DMD), nickel-based superalloy, laser-controlled reaction synthesis, functional graded (FG) intermetallic structures, nickel aluminide

1. Introduction

The range of use of nickel superalloys is diverse and covers gas turbines of air, sea, and road transport and industrial turbines for electro- or gas-pumping stations, rocket motors, automatic spacecrafts, and nuclear reactors. The basic units of the turbines where nickel-based superalloys could be used are combustion chambers, guide blades in nozzles, rotor blades, and turbine disks. It is known that with the temperature rise by every 100° at the turbine inlet, the increase in efficiency is about 3–4%. Therefore, the determination to use these heat-resistant nickel superalloys is reasonable and well grounded [42].

In addition to heat resistance, the materials for the turbine blades are required to be creep resistive to possess lasting plasticity, resistance to gas corrosion and oxidation, high strength, fluidity, and viscosity. This is why the nickel superalloys are mainly used for turbine blades and disks.

Five mechanisms are known for the strengthening of superalloys. They are solid solution, dispersion, grain boundary, deformation, and textural strengthening [3, 42]. The first three ones depend on the alloy nature. In nickel-based alloys, strengthening occurs essentially by the dispersive mechanism due to the γ Ni_3(Al, Ti) phase release. The phase with the $L1_2$–Ni_3Al superlattice is the basis for the fabrication of the promising superalloys of a new generation on the nickel base, owing to the observed anomalous temperature dependence of its mechanical properties. This anomaly is manifested in the form of the yield point increase with the temperature growth within a certain temperature interval. It should be mentioned that such behavior is observed exclusively in alloys with a long-range atomic order, i.e., in superlattice alloys.

Depending on the temperature range necessary for the availability of the γ-solution suitable for the hot deformation of the matrix, the following nickel superalloys are distinguished: deformed, hardly deformed, and nondeformable alloys. There exist several basic groups of the alloying elements for the nickel superalloys:

- Carbide-generating (Cr, Mo, Nb, Hf, and Ta of etc) and oxide-generating (Cr and Al), the latter protect an article against corrosion
- Grain boundary (B, C, and Zr)
- γ precipitates for the (Al, Ti, Hf, and Ta) phases coherent to the austenitic matrix and ensuring the dispersion strengthening. Studies show that their percentage must not exceed

http://dx.doi.org/10.5772/61121

24–26%. The shape of the γ phase particles (spherical, cubic, and lamellar) depends on the nonconformity degree to the lattice parameter of matrix and temperature regimens of synthesis. It influences the mechanical properties of the article.

- Finally, austenitic γ-matrix additives (Co, Fe, Cr, and Mo) are known, which form an fcc lattice with nickel and ensure the solid solution strengthening.

Meanwhile, the formation of σ, μ, and Laves phases resulting in the decrease of the nickel superalloys strength and plasticity is extremely undesirable. It is considered that the basic task for the achievement of the nickel alloy's lasting strength is the ability to control the grain size and orientation, with respect to the size of the article (component). Ensuring the primary grain growth by the oriented crystallization and, if possible, creating single-crystal articles are considered in recent years to be the main line of studies under this technology.

1.1. The nickel superalloy using at the additive technologies

Machining of Ni superalloys by conventional methods is difficult due to rapid work hardening. Therefore, powder metallurgy methods, such as conventional casting, powder sintering, and/or self-propagating high-temperature synthesis (SHS) are not allowed to fabricate Ni superalloy-based functional parts directly.

Recently, additive manufacturing (AM) has been applied to produce Ni superalloy-based parts from corresponded powders. The AM is able to make three-dimensional objects from computer-aided design (CAD) models. Studies in ATs date back to the mid-1980s. Since then, there has been a rapid advance in its development. Actually, selective laser sintering/melting (SLS/M) (DTM and 3D Systems), laser engineered net shaping (LENS) (Sandia Lab), direct metal deposition (DMD) (POM and Optomec), and 3D laser cladding (LC) or 3D laser welding (LW) technologies could be utilized as metal powders and to produce functional parts.

In the case of the SLS/M technology, a layer-by-layer fabrication is realized by powder delivering into the bed substrate. Traditionally, a powder fraction ranging from 20 to 60 μm and a laser beam diameter ~50–70 μm that allows the manufacture of more precise parts and tools are used. In the cases of the very similar LENS, DMD, and 3D LC/LW methods, a coaxial nozzle with the laser beam delivery system, the multichannel powder feeding system, and the numerically controlled multiaxis table are carried out. The particle flow through the nozzle demands particles' sizes to be of more than hundred micron and the beam diameter increasing to some centimeters, so modest precision and increasing productivity could be achieved. Hence, these methods are more suitable for the repair of tools and articles. An electron beam melting (EBM) process is occupying a separate place; i.e., it conducts into vacuum and is characterized to an oxidation and/or nitration absence and good productivity and precision. The 3D LW of a nickel alloy-based wire could be boosted to greater productivity but very modest precision. On the whole, the necessity of AT application is connected with the heightened requirements to the physical and mechanical characteristics of construction materials used in aerospace technologies, and also with the wide prospects opened by the AT for the fabrication of ready-to-serve articles.

The selective laser melting (SLM) of an Inconel 625 (Ni–Cr 21.5%, Mo 9.0%, Nb and Ta 3.6% in wt.%) superalloy using an Nd:YAG pulsed laser to produce thin wall parts with an emphasis on attaining parts with minimum top surface and side surface roughness was obtained [23]. A sample with 9-mm top surface roughness and 10-mm side roughness was produced. A significant fatigue crack propagation in laser rapid manufactured Inconel 625 structures was reported by [7], and the cracks were observed along the growth direction of the specimens, which was predominantly along the [111] plane. A comparison of the SLM and EBM processes for the Inconel 625 superalloy is given at paper by [24]. They identified γ''-Ni_3Nb bct platelets coincident with the NiCr fcc matrix [111] planes. Similar precipitation and grain orientations (textures) were observed by for the SLM fabricated Inconel 718 components too, although the γ'' precipitate platelets were coincident with the NiCr fcc matrix [001] planes rather than the [111] planes. Porous structures of the Inconel-625 by new cross-thin-wall strategy were fabricated at study of [30]. It was found that the yield strength of the fabricated structures followed the power law and decreased from 423 ± 8 MPa for 2.63 ± 0.14% porosity to 226 ± 6.8 MPa for 11.57 ± 0.52% porosity.

An increase in fatigue resistance after the LC process in comparison with wrought and investment cast Inconel 625 was discussed by [44]. The addition of Cr_3C_2 ceramic particles into the Inconel 625 alloy deposited onto a ferrite steel substrate by the LC was analyzed by [45]. As a result, the hard precipitates in the coating microstructure lead to hardness increasing.

[47, 48] described the effect of Al_2O_3 and CeO_2 nanoparticle inclusions into a Ni-based superalloy GH4033 (Ni–Cr 22%; Ti 2.8%; Al 1%; C 0.08%; Fe <1%; Cu, Pb, Bi, Sn, Sb, and As <0.01% in wt.%) during the LC process. The results show that the interface grains, after adding proper nano-Al_2O_3 (1% by mass), grow from epitaxial to nonepitaxial shape gradually, and the columnar dendrites become thinner and denser with cellular shape. Moreover, the dispersive nano-Al_2O_3 particles mainly distribute around cellular substructure and grain boundaries, which prevent the diffusion of alloying elements and restrains the formation of new phase. The addition of 2.0 wt.% nano-CeO_2p showed the most significant improvement effects into the laser-cladded NiCoCrAlY coatings. After adding nano-CeO_2p, an improvement of the microhardness and microstructure uniformity on the cross section and the thermal shock resistance as well were remarked. Results indicate [49] that the hot corrosion resistance of the coatings with nanoparticles is better than that of the one without nanoparticles, among which the one with nano-CeO_2 presented the best hot corrosion resistance. Another effect was observed that the frictional coefficient of the coatings increases and presents the decrease trend with the increase of sliding distance after adding nanoparticles. Moreover [50], the wear rate of the coatings with SiC nanoparticles is only 34.0–64.5% of the coating without nanoparticles.

[60, 6] developed laser induction hybrid rapid cladding process (LIHRC) for the NiCrAlY powder. The preliminary mechanical cryomilling induced the formation of γ′-Ni_3Al and the dissolution of β-NiAl in cryomilled NiCrAlY powder, which in turn was only composed of γ/γ′ (γ: Ni, Cr-rich phase). The oxide products formed on the surface of cryomilled and non-cryomilled coatings were predominantly composed of α-Al_2O_3, Cr_2O_3, $NiCr_2O_4$, and $AlYO_3$, but the mechanical cryomilling a significant improves the oxidation resistance of the NiCrAlY coating by the LIHRC. [43] reported about the SLM process optimization into the NiCr alloy.

http://dx.doi.org/10.5772/61121

The authors observed an unusual growth direction-oriented columnar microstructure of [100] texture (corresponding to the [200] plane). Furthermore, columnar grain growth crossing the melt pools was revealed during the SLM process, and this growth was increasing while the laser scanning speed was decreasing.

The results showed that as the laser scanning speed increased, microhardness decreased at the horizontal surface but increased at the vertical surface, and an increase in yield strength and ultimate tensile strength was observed.

[16] produced a Ni-based superalloy Rene-41 (Ni–Cr 20%, Mo 10.5%, Co 12%, Fe 5%, Ti 3%, Al 1.8%, C 0.12% in wt.%) parts by the DMD process. The columnar grain growth was fixed with well-oriented cellular dendrites and with a primary arm spacing of approximately 35 μm. The additional solution aging at 1065 °C for 4 h and followed by air quenching and aged at 760 °C for 16 h followed by air cooling for the Rene-41 superalloy led to the extensive precipitation of γ, which resulted in high hardness and ductility, and the subsequent alignment and coalescence of γ precipitates induced low-strength [16, 58] reported about crack healing in the Rene88DT superalloy prepared by a laser solid forming after an HIP procedure. [20] reported about good laser weldability of the PM1000 superalloy (Ni–20 Cr, 3Fe–0.5Ti, 0.3Al–$0.6Y_2O_3$ wt.%) account of a dispersion strengthened of yttrium oxide particles.

The Waspaloy (19.5% Ni–Cr, 13.5% Co, 4.3% Mo, 3.0% Ti, 1.3% Al, 0.1% C in wt.%) is an established nickel-based superalloy widely used in the manufacture of compressor discs and combustor cans for the aeroengine gas turbines. [10] developed the DMD process with wire deposit for the Waspaloy. A columnar-dendritic solidification structure with the Ni_3(Al, Ti) precipitate phase (γ) forms with the dendrites growing approximately in the plane of the wall and at an angle of around 30° to the build direction. Mumtaz et al. (2012) developed the SLM process of high-density specimens from the Waspaloy. The laser parameters were determined for a high-power pulsed Nd:YAG laser.

The nickel-based niobium-modified superalloy Inconel 718 (Ni–Cr 19.0%, Fe 18.5%, Nb 5.0%, Mo 3.0% in wt.%) is considered as an important material in aeronautic, astronautic, and nuclear industries in virtue of its excellent high-temperature yield strength, anti oxygenic property, hot corrosion resistance, fatigue resistance, and rupture resistance. [2] used the Inconel 718 powder to fabricate cylinder by the SLM method in an argon and nitrogen environment. As-fabricated cylinders were oriented in the build direction (*z*-axis) and perpendicular to the build direction (*x*-axis) exhibited columnar grains and arrays of γ" (body-centered tetragonal) Ni_3Nb oblate ellipsoidal precipitates oriented in a strong [200] texture. [11] discussed a high-temperature oxidation property in the INT-718 superalloy parts during the SLM process. They determined that the oxidation process was controlled by the outward diffusion of oxide-forming elements and in ward penetration of oxygen. Depending on the applied laser energy density, the coarsened columnar dendrites, clustered dendrites, and slender and uniformly distributed columnar dendrites could form [12]. The optimally prepared fully dense Inconel 718 parts had a uniform microhardness distribution with a mean value of 395.8 $HV_{0.2}$, a considerably low-friction coefficient of 0.36, and a reduced wear rate of 4.64×10^{-4} mm^3/N m in sliding wear tests. [19] developed a laser solid forming (LSF) for the Inconel 718 superalloy and ensured that the predominant γ columnar dendrites directionally growing along the

deposition direction. Primary dendrite arm space measurement revealed spaces of 11.5, 17.5, and 38.0 mm at the bottom, the middle, and the top section of the LSF sample, respectively, in accordance with the Kurz–Giovanola–Trivedi dendrite growth model.

A multiscale finite element model and stochastic analysis was developed to simulate the evolution of the microstructure of the Nb-bearing nickel-based superalloy (INT 718) during a laser additive manufacturing solidification by [26]. The simulations show that a small equiaxed dendrite arm spacing under a high cooling rate and a low-temperature gradient-to-growth rate (G/R) ratio is beneficial in forming discrete Laves phase particles. Therefore, the improvement of hot cracking resistance by controlling the morphology of the Laves phase particles is possible via analyzing the cracking patterns to numerical analyzed. Safdar et al. (2014) developed detailed CFD models that described melt pool flows dominated by Marangoni and buoyancy-driven convection and taken into account an anisotropic-enhanced thermal conductivity during the DMD process for the Inconel 718. For the repair of the nickel-based turbine blades without hot cracking, [55] recommended a laser powder deposition (LPD) process. The 3D finite element model, including parameters of overlapping and bead geometry, has been developed to simulate the multibead pulse LPD process applied to the Ni-based SX turbine blade repair, using the ANSYS code and element reactivation technology.

[55] reported optimal parameters for the DMD of the Inconel 718. With optimal parameters of laser treatment applied, the authors obtained a directional solidification microstructure with an average distance of 5–10 μm between the columnar crystallites. Between the columnar crystal trunk and the columnar crystallite, the microcomposition segregation was observed. Nb, Mo, and Ti concentrated in the crystal trunk. The segregation was sufficiently lower after heat treatment, and segregation ratios were about 1.

[56] precisely developed the DMD process for the filler wire from the Inconel 718 in the Ar environment. The fracture surfaces revealed the presence of both Al_2O_3 and Cr_2O_3 films, although the latter was reasoned to be the main oxide in the IN718. The exposed surface of the oxide film on the fracture surface has poor wetting with the metal and thus may nucleate some intermetallic compounds, such as the Laves, Ni_3Nb-d, Nb-rich MC, and c0 compounds.

[4] obtained the LC process-induced microstructural characteristics for the INT-738 (Ni–Cr 16%, Co 8.3%, Ti 3.38%, Al 3.4%, W 2.6%, Ta 1.7%, Mo 1.7% in wt.%) superalloy with coarse columnar grains in the range of about 56–158 μm in diameter, and the secondary dendritic arm spacing is about 1.7 μm. The IN-738 alloy after the LC was a supersaturated γ solid solution, but any precipitation of γ particles from the γ matrix was effectively suppressed. [21] reported about liquation cracks in the IN738LC alloy after the LW which were associated with grain boundaries constituents such as γ–γ′ eutectic, MC carbide, Cr–Mo boride, and Ni–Zr intermetallic. [5] informed about crack-free laser welds of the INT-738 nickel-based superalloy under preheating at approximately 800°C. [59] informed about minimization of the boundary liquation and interface cracking styles into the Inconel 738 after the DMD. With an extra high-temperature gradient and cooling rate during the deposition process, laser deposition is able to produce directional solidification structure and to control the microstructure.

The LW of the cast Ni-based superalloy K418 (Ni–Cr 12.54%, Mo 4.59%, Al 5.81%, Nb 2.35%, Ti 0.97%, Fe 0.17%, C 0.13%, B 0.13% in wt.%) turbo disk and alloy steel 42CrMo shaft were conducted in [18]. It was remarked that the structure of the laser-welded seam was extremely heterogeneous and consisted mainly of FeCr0.29Ni0.16C0.06 austenite in a form of solid solution dendrites with inclusions of Ni_3Al γ phase and Laves particles, as well as with MC globular or needle-shaped carbides distributed by boundaries between the dendrites.

[29] reported about the LW of the cast nickel-based superalloy K418. Microstructures consisted mainly of austenite solid solution dendrites but also had fine-dispersed $Ni_3(Al, Ti)$ γ phase, MC needle-shaped carbides, and Nb, Ti, and Mo-enriched particles distributed in regions between the dendrites. The microcracks were caused by the liquation of low melting point eutectics in the heat-affected zone (HAZ) and at the grain boundary.

The γ precipitation in the primary γ' of the new Ni–Co-base disc superalloy, TMW-4M3 (Ni–Co 25%, Cr 13.5%, Mo 2.8%, Ti 6.2%, Al 2.3%, W 1.2%, C, B, Zr ~0.02–0.03% in wt.%), was studied by [51]. The size of these tiny particles was unlikely to change after a two-step sagging treatment, but a significant growth was detected after creep rupture at 725°C under various stresses. [14] developed a homogenized, activation energy-based crystal plasticity model for the single-crystal Ni-based superalloys that can be implemented in simulations of polycrystalline aggregates. [57] conducted the LENS process optimization for the 84Ni14.4Cu1.6Sn powder alloy. Thick-wall parts with thickness ranged from 20 to 25 mm were fabricated.

Acharya et al. (2014) presented a comprehensive thermal, fluid flow, and solidification model that can predict the temperature distribution and flow characteristics for the processing of the CMSX-4 (Ni–Cr 6.5%, Co 9.6%, W 6.4%, Ta 6.5%, Al 5.6%, Re 3%, Ti 1%, Mo 0.6%, Hf 0.1% in wt.%) alloy powder through the scanning laser epitaxy (SLE) process. The fabrication of equiaxed, directionally solidified, and single-crystal (SX) deposits of the nickel-based superalloys was successfully using a fast-scanning laser beam. Under temperature gradients at the leading and trailing edges of blades are the order 2.9×10^5 and 10^4 K/m, respectively. In the empirical values for several microstructural characteristics such as the primary dendrite arm spacing of 10–30 μm in the deposit region, unsteadiness of the columnar-to-equiaxed transition criterion value was found, and the oriented-to-misoriented transition criterion is obtained.

Last decade, specific types of studies were devoted to combination of the self-propagated high-temperature synthesis (SHS) and rapid prototyping approaches, which allow synthesized and 3D part fabricated in situ nickel aluminide phases [13, 28, 31, 32, 35, 37]. The experimental parameters controlling the ignition step such as an ignition time, a width of the exothermic reaction zone, and an adiabatic temperature were calculated as a function of initial stoichiometry for different Ni_xAl_y phases. The increase in Al powder content resulted in the rise in adiabatic temperature and the morphology change of nickel aluminide compounds from needlelike to blocky.

[37] and later [32] showed that the laser reaction sintering of the NiAl consists of a complex reaction with several sequential steps. First, the Al-rich compounds $NiAl_3$ and Ni_2Al_3 are formed. Subsequently, these phases react with Ni to form NiAl. In the stage of bulk combustion, Ni continuously dissolved into liquid Al(Ni) solution and transformed the NiAl phase

and a lot of heat. Finally, the Ni reacted with NiAl phase and formed the terminal product–Ni_3Al phase.

Despite the mentioned above serious success in the field of the complex functional articles fabrication out of prepared nickel superalloys, it is still actual to develop new classes of solid, nonbrittle, corrosion- and wear-resistant, and chiefly heat-resistant materials, for instance, on the basis of NixAly phases. There also exists an actual need to generate gradient and laminar structures of the nickel superalloys reinforced by the nickel aluminides, which can be used for production of components and elements for the rocket–space technology. Some approaches to the layered synthesis of intermetallide phases of the NixAly type and gradient of mechanical properties in the obtained laminar structures will be reviewed below. The major task of the work is to develop the basis for the manufacturing of laminar materials with predetermined properties by the different AT approach conditions and to compare conditions required for this.

2. Experimental scheme layerwise fabrication of the FG nickel aluminide's structures

Earlier, we experimentally approved the layerwise SLM and DMD processes in the Ni + Al system [9, 13, 35, 41] and theoretically substantiated [53] the approach, where the strengthened intermetallides are created directly within the laser-assisted AM process in the Ni metallic matrix due to the synthesis reaction.

The LI initiates a chemical reaction between the particles in the powder mixture of stoichiometric composition (Ni + Al, Ni + Ti, Ni + Ti + Al), and this leads to intermetallic phase composition. Moreover, deviation from stoichiometric ratios causes the aggregation of this excess on the matrix of nickel superalloy.

Earlier, we remarked [39, 40] that the LI-controlled intermetallide synthesis reaction is advantageous because it provides uniform and fine distribution of the inclusions and makes the superalloy matrix more stable, while an additional input of energy from exothermic reaction allows using less energy-requiring laser sources.

In addition to activating the synthesis reaction [37, 39, 53], LI also accelerates the directed crystallization and customizable controls the microstructure's properties.

Controlling the thickness of the powdered layer (i.e., the reaction zone volume) during the additive manufacturing process (compare the HAZ under the SMS vs. the DMD processes) can affect the character and direction of the exothermic synthesis reaction and activate the scalable process of directed solidification. Furthermore, the laser power and scanning speed also affect the melting-crystallization conditions.

Functionally graded structures (FGS) and FG articles fabricated by applying complex and dissimilar materials ensure the specific properties of the final product. The manufacturing of 3D FG objects by the 3D LC and/or LDMD is one of the most promising techniques capable of

http://dx.doi.org/10.5772/61121

meeting various industrial challenges [27, 36, 41]. This approach permits new freedoms in design and manufacturing, thus allowing, for example, to create an object with the desired shape, internal structure, and engineering composition, including the appropriate physic-mechanical properties, within a single-step fabrication process.

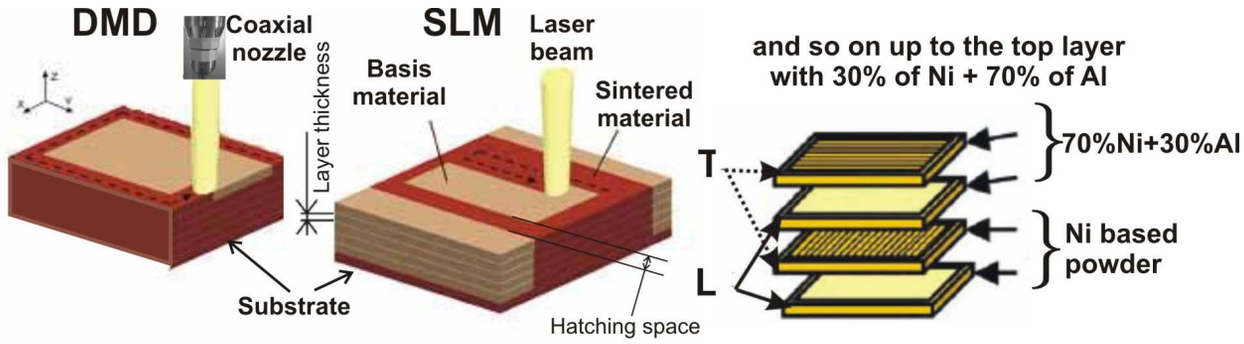

Figure 1. Schematic of the multicomponent-graded structure fabrication by the DMD and SLM processes. Longitudinal —L; transversal—T.

The next powders were used for the FGS fabrication via the LDMD. The aluminum powder had 99 wt.% of Al (TLS Technik GmbH&Co.). The NiCr superalloy Diamalloy 1005 (Sulzer Metco Co.) was used as the Ni powder, which had the following chemical composition: Cr—21.5, Fe—2.5, Mo—9, Nb 3.7 wt.%, bal.–Ni. The powder particles were mainly spherical with the size of ~80–100 μm for 95% of them. The steel substrates of a square shape with a width of 65 and 5 mm height were used. The Diamalloy is equivalent to the Inconel 525 alloy, which was studied earlier in the DMD process [6].

The LDMD method for the FGS fabrication used in the present study is schematically presented in Fig. 1 and was proposed us early [38]. The hatching distance was 2 mm, the layer thickness was ~1 mm, and the powder feeding rate was ~10 g/min. The layers were made out of Ni-based (Diamaloy) and Al powders on a related substrate by the following strategy: the first two layers were of pure NiCr, the next two consisted of 70% NiCr + 30% Al, the third couple of layers were of 50% NiCr + 50% Al, and lastly the upper 7th and 8th layers had the ratio of 30% of NiCr + 70% of Al. Each second layer was formed on the bottom layer after its turning by 90°. For the Fe–Al system, this scheme was successfully approbated at [39, 40]. Argon was the carrying gas. Laser scanning speed was 500 mm/min, laser power varied within the range of 800–1200 W, and laser beam spot diameter was 3 mm. The first channel of the feeder with the Diamaloy powder had a gas flow rate of approximately 20 l/min, while the second one with the Al powder was ~10 l/min.

The following powders were used for the SLM process of FGS fabrication (Fig. 1) in the Ni–Al system. The aluminum powder used was AMDRY 355 (Al + Si 12 wt.%, –45 μm) and nickel powder was Metco 56C-NS (Ni > 99.5 wt.% –75 + 10 μm), which were supplied by Sulzer Metco, GmbH. The scheme of alteration for Ni- and Al-based powders (Ni + Al = 3:1; 1:1; 1:3 wt.%) during the process using SLM approach (Fig. 1) was analogical to the one mentioned above for DMD process.

Granulomorphological analysis of the micron sized powders was carried out by the optical granulomorphometer ALPAGA 500 NANO. The SLM process was performed on the Concept M3 setup (Germany), and the DMD process was realized with the aid of the HAAS 2006D (Nd^{+3}:YAG, 4000 W, cw) with the laser beam delivery system, powder feeding system, coaxial nozzle, and numerically controlled five-axes table (Fig. 1). The FGS results after DMD and SLM processes were compared with each other and with the SLM process of the Ni85Al15 nickel superalloy powder produced by the JSC Polema Ltd. (Tula, RF). The Ni85Al15 powder was represented by a 20- to 63-μm fraction and containing >95 wt.% of intermetallic Ni_3Al phase. Results of the LAM processes are shown in Fig. 2.

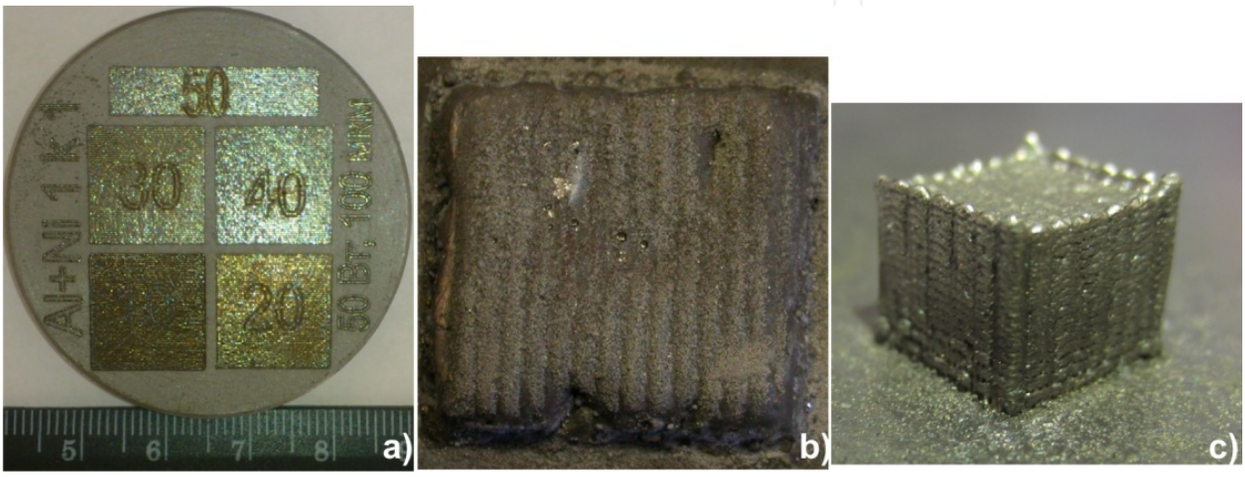

Figure 2. Appearance of the SLM and DMD processes: (a) SLM in Al + Ni = 1:1 system, three layers, hatch distance 0.1 mm; (b) FGS in Ni–Al after DMD; (c) DMD of cube (5 mm^3) from the Ni85Al15 powder.

3. Laser DMD of FG layered nickel aluminides

The optical metallography after FGS fabrication via DMD process is presented in Fig. 3.

The photographs are selected in order to show the characteristic microstructures based on the lower (a1, a2), middle (b, b1), and upper (c, c1) parts of the FGS, i.e., where the proportions of the powdered Ni + Al ≈ 3:1; 1:1 and 1:3 by weight ratios were comprised. Under large magnification, these layers are presented on the inserts a1 and a2 for bottom, b1 for panel b, and c1 for panel c. In the lower layers in the photo (Fig. 3a1), a columnar dendrite pattern was observed, which characterized the high-speed quenching of the NiCr superalloy practically without Al additive participation (compare with [6]). The dendrite growth direction (Fig. 3a1) is stipulated for maximum heat dissipation to the massive substrate. We connect superfluous crackability in Figs. 3a1 and a2 (shown by arrows) with the nonoptimal selection of the increment height from one layer to the next. At the top layers (Figs. 3a1 and b), the microstructure radically changes. In the middle (bottom of Fig. 3a2 or Figs. 3b–b1), there is a cellular and rosette microstructure, which can testify to the equivalence of the heat dissipation speeds in different directions from this area. The upper layers (Figs. 3c–c1) have a needle-shaped

http://dx.doi.org/10.5772/61121

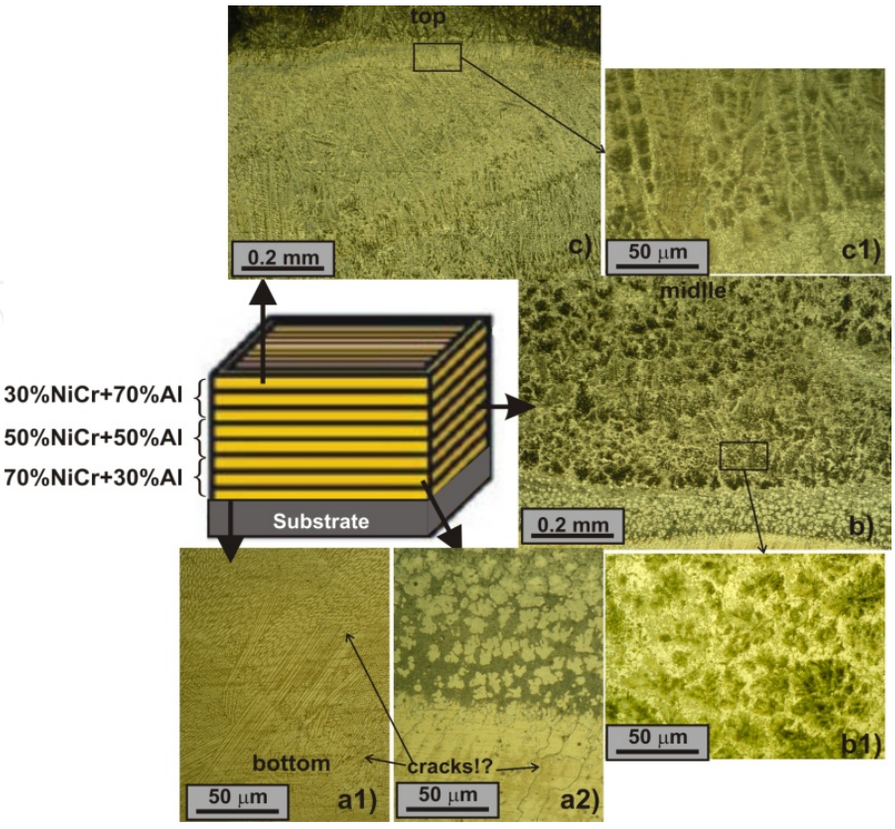

Figure 3. OM micrographs showing the typical microstructures of 3D laser clad coating of NiCr–Al multilayer system: (a) bottom layers ~2–4 mm from substrate; (b) middle layers ~4–6 mm from substrate; (c) top layers ~6–8 mm from substrate.

microstructure with the impregnations of intermetallide phases. At the middle layers, we also observed the triple eutectic structure, which consists of a γ-solid solution on the nickel basis, an α-solid solution on the chromium basis, and also a γ-solid solution on the basis of the Ni_3Al intermetallic compound in the middle and NiAl intermetallide phase above. By the boundaries of the (α + γ + γ) triple eutectic colonies, the two-component eutectic is arranged, which includes the γ-solid solution on the Ni basis and $AlCr_2$ intermetallide phase.

The results of a microhardness measuring are shown in Fig. 4. If the microhardness is equal to 500–550 $HV_{0.1}$ near the base, then it unevenly grows and reaches up to 650–750 $HV_{0.1}$. We connect the separate dips in the microhardness value in the bottom layers (up to 2 mm from the substrate; Fig. 4) with the superfluous cracks, and in the top layers with the indentor entry into the Diamalloy 1005 matrix. On the whole, the measured microhardness values considerably exceed other researchers' data (200–250 $HV_{0.1}$ for the Inconel 625 after the DMD process by [6]).

The XRD pattern of a transverse section after the DMD in the NiCr–Al system is shown in Fig. 5. We can draw the following basic conclusions. After the FGS fabrication, the free nickel and aluminum are practically absent, i.e., it has completely interacted with the Ni_3Al and NiAl intermetallic phase formation. This distinguishes our results from the data of [6], which fixed both the free nickel, γ-, and δ-Ni_3Nb phases under similar DMD regimens with the subsequent

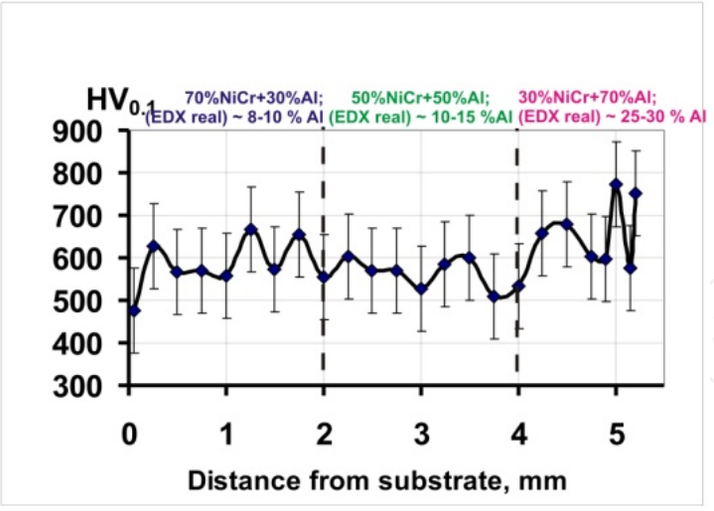

Figure 4. Microhardness distributions of NiCr–Al FG multilayer system.

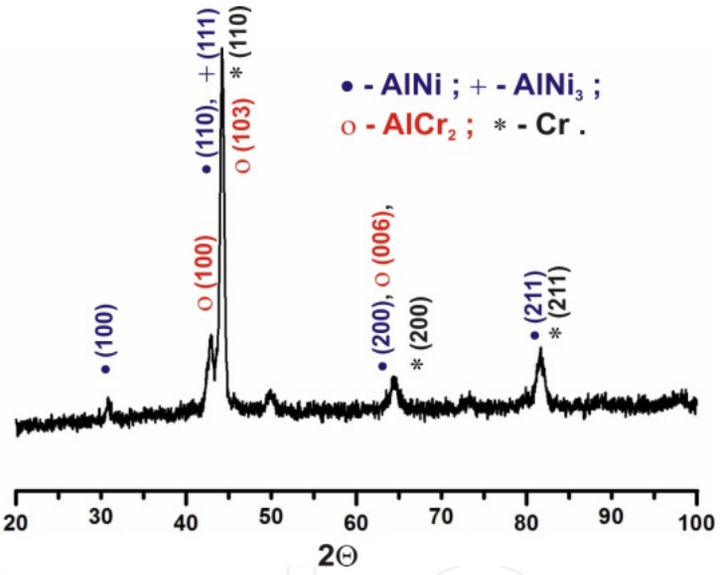

Figure 5. X-ray diffraction patterns of NiCr–Al DMD multilayer system.

annealing. Since the intensity lines of free chromium practically coincide with the intensity lines for the intermetallic compound-AlNi, asserting unambiguously about the free Cr presence is impossible. Meanwhile, the presence of intermetallic phase of $AlCr_2$ is possible.

Fig. 6 shows the SEM data in the bottom, middle, and top layers of the FGS after the layerwise DMD in the NiCr–Al system. For clearness, Figs. 6b–c are similar to Figs. 3b–c, and inserts in Figs. 6b1–c1 are similar to inserts in Figs. 3b1–c1. It is evident that its microelement composition (S1 and S2) practically repeats the initial Diamalloy 1005 composition plus 3.37% wt of Al (see Table 1). By the element relationship in the S3 and S4 areas (Fig. 6b), we have the nickel superalloy matrix depleted by Al. The existence of the metastable Ni_5Al_3 intermetallic phase is possible, on the boundaries of which free Cr extraction has been observed (see Fig. 6b1 and

http://dx.doi.org/10.5772/61121

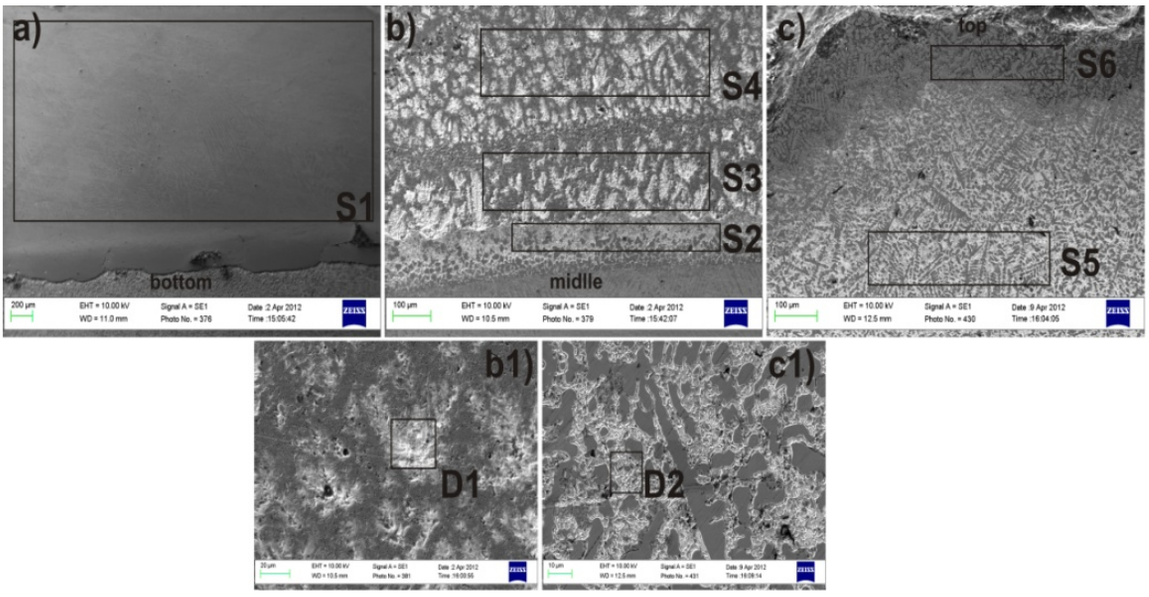

Figure 6. SEM micrographs showing typical solidification microstructures of the bottom (a), middle (b), and top (c) deposited layers with places of the EDS analysis of NiCr–Al multilayer gradient (see Table 1).

D1 area also). Finally, a dendritic structure in Fig. 6c (S5 and S6) clearly shows the intermetallide nature of the Ni_3Al phase. Fig. 6c1 corresponds to Fig. 3c1. We can assert that in the upper layers, the synthesis of the Ni_3Al intermetallide phases (S5–S6 and D2) occurs, as well as a precipitation of the $AlCr_2$ intermetallide phase on the grain boundaries. With sufficient carbon (up to 5 wt.%) and oxygen (up to 3 wt.%) content, we connect with the possibility of their hit from the environment, although the XRD pattern does not fix these elements. [46] informed that the high-temperature oxidation was a great problem after the 3D LC too.

Spectrum	C K	O K	Al K	Si K	Cr L	Fe L	Ni L
S1	1.88	1.47	-	1.03	38.99	1.28	55.35
S2	3.38	1.91	3.37	1.07	51.61	-	37.89
S3	5.66	2.82	2.02	2.94	71.61	1.24	15.71
S4	2.97	2.99	5.02	1.11	11.37	65.32	22.6
S5	3.38	1.41	28.94	0.41	14.04	-	51.35
S6	5.79	1.26	30.48	0.51	18.61	-	43.24
D1	2.89	-	12.24	0.78	50.94	-	33.15
D2	2.24	1.46	34.75	-	6.29	-	55.26

Table 1. EDS data by Fig. 6.

Nevertheless, the main question is Where is aluminum after the layerwise deposition? According to the flow data, in the middle layers, we had to contribute up to 50% of Al, while

in upper ones—up to 70% of Al. Meantime, given EDS and XRD data, there was about 10–15% of Al in the middle layers and no more than 30% in the top. Future studies must be conducted to answer this question.

Thus, under the layerwise LDMD in the NiCr–Al system, the formation of the Ni_3Al intermetallic compounds was observed. The applicability of the LDMD for creating a functional gradient and building of Ni_xAl_y intermetallic structures into the nickel superalloy matrix has been experimentally studied. The microhardness values from 500 to 750 $HV_{0.1}$ were achieved, which precisely connected with the intermetallide phase's presence in the NiCr matrix.

4. SLM of the FG-layered nickel aluminides

Optimal regimes for the SLM process in the Ni–Al = 1:1 system were as follows: 100, 120, and 140 mm/s for 100 W of the LI and 160, 200, and 240 mm/s for 150 W (Fig. 2a). Optimal regimes for SLM in the Ni–Al = 3:1 system were 160 and 200 mm/s for 150 W. At last, optimal parameters of SLM of prealloyed intermetallic phase (Ni85Al15 powder) were proved to be 120 and 160 mm/s under 150 W.

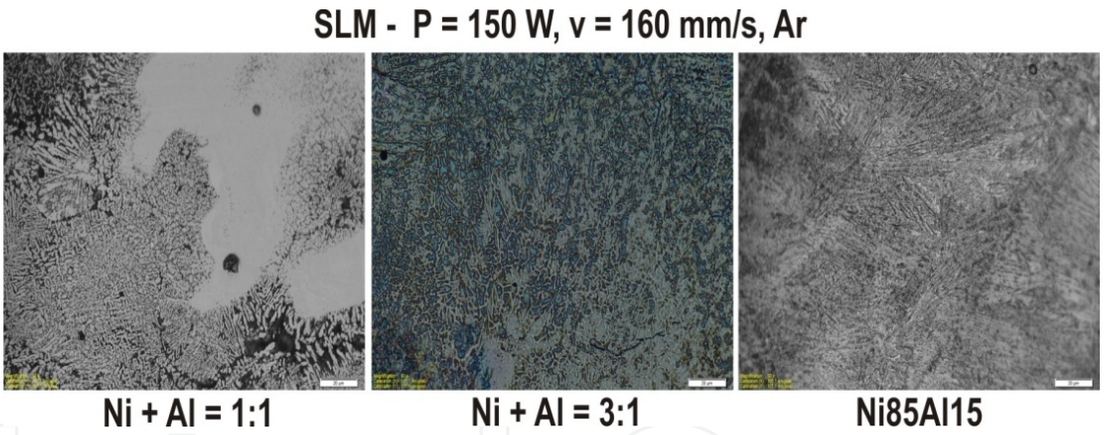

Figure 7. Comparative optical metallography after the SLM in Ni + Al = 1:1 (a); Ni + Al = 3:1 (b), and prealloyed Ni85Al15 (c). Magnification is ×500.

The most acceptable from methodical position SLM regime was chosen for all mixtures (P = 150 W, v = 160 mm/s) to carry out a more careful analysis, with subsequent comparison and experimental studying of FGS possibilities via the SLM process in the Ni–Al system with the variable contents of elements. From the analysis in Fig. 7, it is clear that crack's generation and porosity are observed in all the cases. A recommendation for future studies is to conduct the SLM process in a camera with the temperature increased (see the SLM results of the NiTi at [39, 40]. Dendrite structure obtained after melt cooling is clearly visible.

SEM images (Fig. 8) show fine dendrite structure with different grain orientations. Also, we can mention cracks and pores (Figs. 8a, b). Areas S1, S2, and S3 are the places where EDS analysis (Table 2) was carried out. Microelement analysis ensured that we really handle with

http://dx.doi.org/10.5772/61121

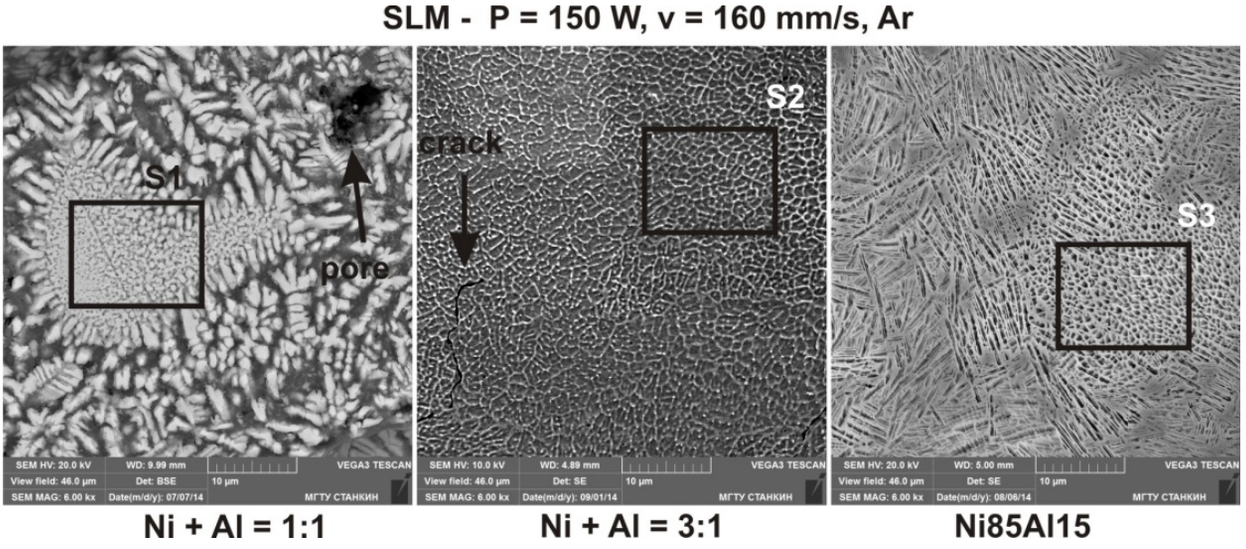

Figure 8. Comparative SEM after SLM in Ni + Al = 1:1 (a); Ni + Al = 3:1 (b); and prealloyed Ni85Al15 (c). Magnification is ×6000.

intermetallic Ni_3Al phase (Fig. 8c and Table 2—S3), intermetallic Ni_3AlSi phase (Fig. 8b and Table 2—S2), and intermetallic NiAlSi phase (Fig. 8a and Table 2—S1). The recent results obtained for kinetics of coarsening of γ precipitates in Ni superalloys have shown that Si additive varies both magnitude and sign of coherency strains between the precipitate and the matrix.

	S1	S2	S3
Element			
Al	53.55	21.94	12.20
Ni	38.07	74.83	87.80
Si	8.38	3.23	-
Total:	100.00	100.00	100.00

Table 2. EDS data by Fig. 8.

X-ray diffraction patterns showed (Fig. 9) clear reflections from AlNi phase, characteristic for JCPDS card no. 20-0019, from metastable intermetallic Ni_3Al_2 phase (JCPDS, card no. 14-0648), pure aluminum (JCPDS, card no. 01-1180), and $Al_{3.21}Si_{0.42}$ (JCPDS, card no. 41-1222).

X-ray phase analysis was supported by the EDS data. Near the high-intensity Al lines, we noticed intermetallic AlNi and Al_3Ni_2 phases too. They were synthesized during the laser-controlled SHS process. It is known that metastable Al_3Ni_2 phase has matching with Ni_3Al in whole intensity lines, so the question about Ni_3Al phase presence is open. Great solubility of Si in NiAl and Ni_2Al_3 phases can provoke improvement of strength in these intermetallic phases.

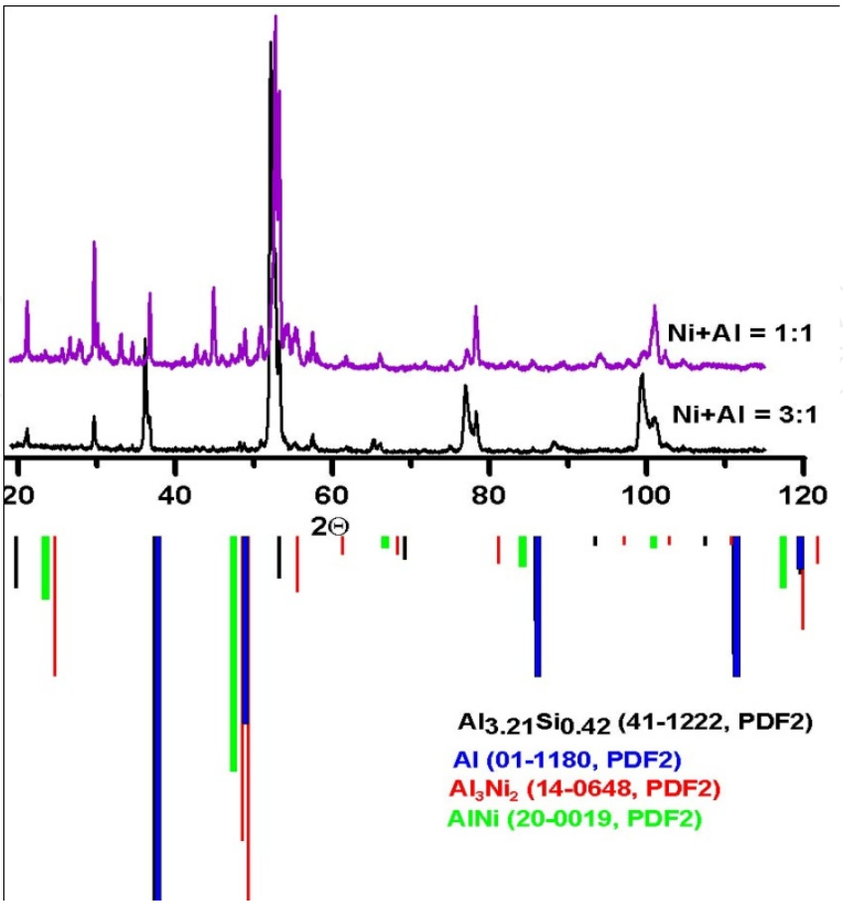

Figure 9. Comparative XRD pattern after SLM in the Ni + Al = 1:1 - (8 layers, violet) and Ni + Al = 3:1 systems (10 layers, black color line). SLM regimen is according to Fig. 7.

Hence, we have shown that layerwise SLM in Ni–Al system with alteration of Ni and Al content allows to fabricate Ni_3Al intermetallic compounds too. Applicability of SLM for creating FGS and building Ni_xAl_y intermetallic structures in nickel superalloy matrix has been experimentally studied.

5. Laser DMD and SLM of prealloyed nickel aluminide

LDMD and SLM of nickel superalloy (Ni85Al15) were successfully realized (Figs. 2c and 7c–8c) [15, 25]. The measured microhardness (Fig. 10) of the laser deposited 3D part (cube) grows from the substrate to the top irregularly. We believe this to be connected with a local hardness increase in the intermetallic phase locations. We connect certain microhardness dip ($HV_{0.1}$ 350) to the indentor hip on the layer boundary. As a whole, the microhardness values correspond to the similar measurements on the nickel aluminides after the DMD and LENS processes, but some are lower than the microhardness of the laser cladded NiAl phase [6, 52].

The qualitative X-ray analysis results are presented in Fig. 11. After the multilayer laser deposition, we have stronger lines, which are located at the angles of ~2θ of 51.4° and 52.1°,

http://dx.doi.org/10.5772/61121

which directly correspond to (111) γ-Ni_3Al and metastable (110) Ni_2Al intermetallic phases. We can propose that probably iron substrate with an interplanar spacing (110) is visible also. The crystal-lattice orientation of the γ-Ni_3Al has preferred direction [111]. On taking into account all the peaks mentioned above, it is reasonable to conclude that this XRD pattern (Fig. 11) best of all coincides with the set of the lines for the Ni_3Al intermetallide. It means that during the LDMD process, this phase remains in a stable state, which corresponds with the aim of our study.

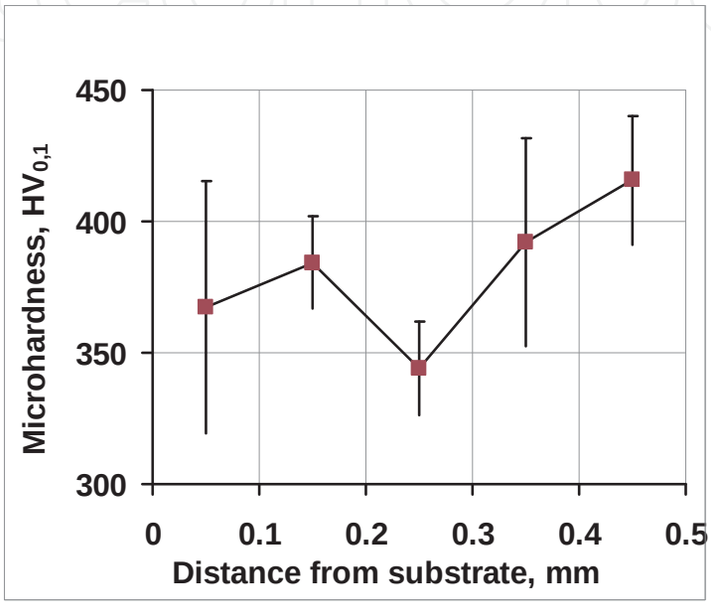

Figure 10. Microhardness distributions of the Ni85Al15 after the multilayer DMD.

SEM images with EDX analysis of the micro- and substructures are shown in Fig. 12. Microstructure study showed that the length of the main dendrite arms was about 15–20 μm, but the grain size was 40–50 μm (Fig. 12b). The secondary dendrite arms varied between 5 and 8 μm. Such structure refinement is connected with a high-speed crystallization from the melt. The dendrite orientation is mainly coplanar with the image; nearby, it is perpendicular to the image plane. Cracks (Fig. 12a) between the second and the first layers were formed on the cooling stage. This broken type indicates the shift nature of plastic deformation under melt cooling.

It should be pointed out that the microstructure mostly consists of columnar-type dendrites, which grew epitaxially from the substrate. Moreover, the growth direction of the columnar dendrites was tied to the laser scanning direction. From Fig. 12b, it is seen that the primary dendrites have almost the same orientation throughout the sample. In contrast, Fig. 12b shows that for the top and the bottom layers, the growth direction of the columnar dendrites changes by 90° in every layer. Hence, during the solidification of the melt pool, cooling mostly occurs via the substrate and the deposit. This leads to the directional growth of the grain counter to the heat dissipation and subsequently the formation of the columnar grains.

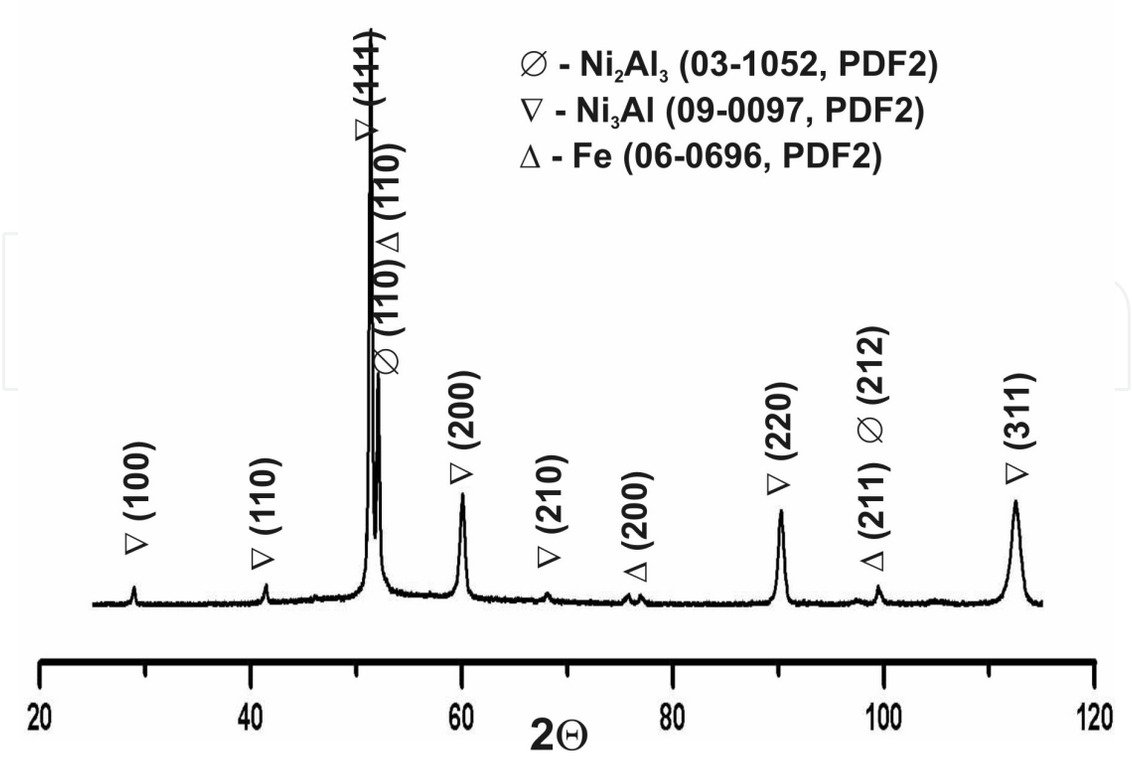

Figure 11. X-ray diffraction pattern of the Ni85Al15 after the multilayer DMD.

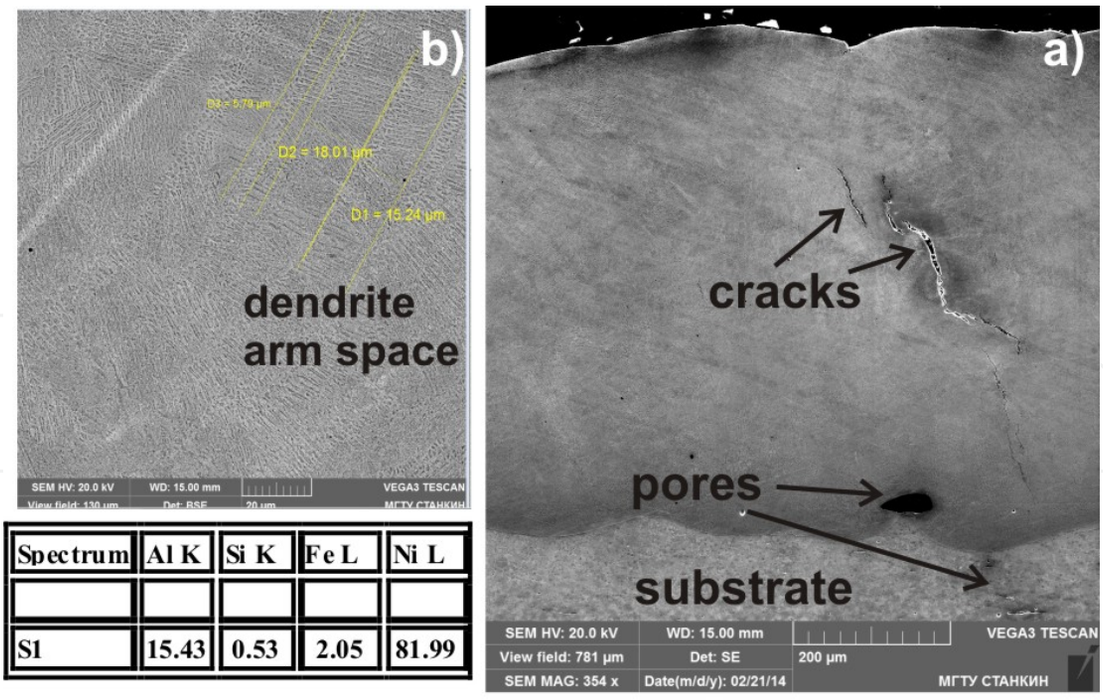

Spectrum	Al K	Si K	Fe L	Ni L
S1	15.43	0.53	2.05	81.99

Figure 12. SEM micrographs showing typical solidification microstructures of the laser deposited layers with the laser scanning speed of 600 mm/min, 250 W, and 9 g/min. Step between the layers was 200 μm, and EDS analysis date (table) from whole image square.

http://dx.doi.org/10.5772/61121

The EDS data of the composition distribution from the cladding layer to the substrate are shown in Fig. 12 into inserted table. It can be found that the matrix element Fe enters into the first cladded layer. The dilution of the substrate elements was notable with the increasing of the laser power density. Evidently, the reason is the accelerating diffusion processes for iron and the excessive overheating of the substrate at the high-power density.

6. Conclusion

The aim of this chapter was to emphasize capabilities and performances of the SLM and LDMD processes for FG part fabrication. Comparison of LDMD and SLM processes ensures that a more precise localization of laser beam is the preferred alternative for the fabrication of precise parts in the SLM process compared with the LDMD process. However, DMD warms up a powder volume more deeply, so an FGS with more homogeneous microstructure is being formed. On the other hand, the absence of initial powder around the manufactured objects leads to steep slopes on their edges after the DMD. This decreases the part's accuracy. In both cases, additional thermal heating of the synthesis zone is preferred.

The LDMD and the SLM of single layers and 3D objects of the Ni_3Al intermetallic were successfully prepared. Good metallographic characteristics and interface bonding were obtained. The fabricated microstructure consisted of γ-Ni_3Al. At the nickel and aluminum boundary, the NiAl and the Ni_3Al intermetallic phase layers are obtained, which possess high-strength characteristics. It is discovered that the concentration of NiAl and Ni_3Al phases is heterogeneous. Mechanisms of nickel aluminide intermetallic compound formation in the zone of the LDMD and SLM are studied. Thermal time parameters of the laser treatment required for the formation of these intermetallide compounds, structurally uniform and of maximum width, are revealed in the work.

7. Outlook

In controlling a multilayer structure, hardness can provide more scalabilities and customizations to apply the 3D FGM in aerospace and nuclear industries by changing the composition of the powder and by using proper CAD modeling. The studies on controlling the residual stresses and revealing LAM conditions for large and/or high-precision samples are provoking further interest.

The results of these studies can be the basis for the development and manufacture of a new class of construction materials—laminar intermetallide composites. From this aspect, nickel–aluminum alloys have a special interest due to their use for the production of units and components for aviation and space equipment, such as fuselage coverings of aircrafts, fuel injectors, screws components, components of the rocket engine nozzle, etc.

Thus, the study by means of the gradient LDMD and SLM in the Ni–Al system under different treatment regimens allowed us to discover that within the wide concentration interval of the

Al_xNi_y phase existence, the synthesis of several intermetallic compounds into nickel matrix is observed. These intermetallic compounds have an interface and differ by their element composition.

Acknowledgements

The authors are grateful to Mr. Missemer F. (DIPI, ENISE, France) for the 3D laser cladding processing, Kuznetsov S. (LPI), PhD, for the X-ray analysis data. Nazarov A., PhD, and Kotoban D. would like to thank the support of the Russian Science Foundation (grant no. 14-19-00992). Ms. Kakovkina N. is separately grateful for the financial support of the Russian Foundation of Basis Researches (grant no. 14-29-10193 ofi-m).

Author details

Igor V. Shishkovsky[1,2*], Aleksey P. Nazarov[2], Dmitry V. Kotoban[2] and Nina G. Kakovkina[1]

*Address all correspondence to: shiv@fian.smr.ru

1 Lebedev Physical Institute (LPI) of Russian Academy of Sciences, Samara Branch, Samara, Russia

2 Moscow State Technological University, STANKIN, LIAT, Moscow, Russia

References

[1] Acharya R., Bansal R., Gambone J. J., Das S. (2012) A coupled thermal, fluid flow, and solidification model for the processing of single-crystal alloy CMSX-4 through scanning laser epitaxy for turbine engine hot-section component repair (Part I and Part II). *Metallurgical and Materials Transactions B.* doi: 10.1007/s11663-014-0117-9.

[2] Amato K.N., Gaytan S.M., Murr L.E., Martinez E., Shindo P.W., Hernandez J., Collins S., Medina F. (2012). Microstructures and mechanical behavior of Inconel 718 fabricated by selective laser melting. *Acta Materialia* Vol. 60, pp. 2229–2239.

[3] Canh R.W., Haasen P (1983). *Physical Metallurgy*. 3rd revised and enlarged edition. North-Holland physics publishing, Amsterdam, Oxford, New York, Tokyo, Part 1–2 and 3, 2050 p.

[4] Chen J., Xue L. (2010) Process-induced microstructural characteristics of laser consolidated IN-738 Superalloy. *Materials Science and Engineering A.* Vol. 527, pp. 7318–7328.

[5] Chiang M.F., Chen C. (2009). Induction-assisted laser welding of IN-738 nickel–base superalloy. *Materials Chemistry and Physics*, Vol. 114, pp. 415–419.

[6] Dinda G.P., Dasgupta A.K., Mazumder J. (2009) Laser aided direct metal deposition of Inconel 625 superalloy: microstructural evolution and thermal stability, *Materials Science Engineering A,* Vol. 509, pp. 98–104.

[7] Ganesh P., Kaul R., Paul C.P., Tiwari P., Rai S.K., Prasad R.C., Kukreja L.M. (2010) Fatigue and fracture toughness characteristics of laser rapid manufactured Inconel 625 structures. *Materials Science and Engineering A,* Vol. 527, pp. 7490–7497.

[8] Gill A, Telang A., Mannava S.R., Qian D., Pyoun Y.-S., Soyama H., Vasudevan V.K. (2013). Comparison of mechanisms of advanced mechanical surface treatments in nickel-based superalloy. *Materials Science and Engineering A,* Vol. 576, pp. 346–355.

[9] Gureev D.M., Petrov A.L., Shishkovsky I.V. (1999) Formation of intermetallics phases under laser sintering of powdered SHS compositions, *Proceedings of SPIE.* Vol. 3688-36, Jan. pp. 237–242. doi:10.1117/12.337516.

[10] Hussein N.I.S., Segal J., McCartney D.G., Pashby I.R. (2008) Microstructure formation in Waspaloy multilayer builds following direct metal deposition with laser and wire. *Materials Science and Engineering A,* Vol. 497, pp. 260–269.

[11] Jia Q., Gu D. (2014a) Selective laser melting additive manufactured Inconel 718 superalloy parts: high-temperature oxidation property and its mechanisms. *Optics and Laser Technology,* Vol. 62, pp. 161–171.

[12] Jia Q., Gu D. (2014b) Selective laser melting additive manufacturing of Inconel 718 superalloy parts: densification, microstructure and properties. *Journal of Alloys and Compounds,* Vol. 585, pp. 713–721.

[13] Kamashev A.V., Panin A.S., Petrov A.L., Shishkovskii I.V. (2001). Laser-controlled synthesis of nickel-aluminum intermetallic compounds. *Technical Physics Letters.* Vol. 27, Number 6, pp. 498–499. doi: 10.1134/1.1383837.

[14] Keshavarz S., Ghosh S. (2013) Multi-scale crystal plasticity finite element model approach to modeling nickel-based superalloys. *Acta Materialia,* Vol. 61, pp. 6549–6561.

[15] Kotoban D., Grigoriev S., Shishkovsky I. (2014). Study of 3D laser cladding for Ni85Al15 superalloy. *Physics Procedia.* Vol. 56, pp. 263–269.

[16] Li J., Wang H.M. (2010). Microstructure and mechanical properties of rapid directionally solidified Ni-base superalloy Rene_41 by laser melting deposition manufacturing. *Materials Science and Engineering A*, Vol. 527, pp. 4823–4829.

[17] Li J., Wang H.M., Tang H.B. (2013) Effect of heat treatment on microstructure and mechanical properties of laser melting deposited Ni-base superalloy Rene_41. *Materials Science and Engineering A,* Vol. 550, pp. 97– 102.

[18] Liu X.-B., Yu G., Guo J., Gu Y.-J., Pang M., Zheng C.-Y., Wang H.-H. (2008). Research on laser welding of cast Ni-based superalloy K418 turbo disk and alloy steel 42CrMo shaft. *Journal of Alloys and Compounds,* Vol. 453, pp. 371–378.

[19] Liu F., Lin X., Leng H., Cao J., Liu Q., Huang C., Huang W. (2013). Microstructural changes in a laser solid forming Inconel 718 superalloy thin wall in the deposition direction. *Optics and Laser Technology,* Vol. 45, pp. 330–335.

[20] Lemmen H.J.K., Sudmeijer J., Richardson I.M., Zwaag S. (2007). Laser beam welding of an oxide dispersion strengthened super alloy. *Mater Sci*., Vol.42, pp. 5286–5295.

[21] Montazeri M., Ghaini F.M. (2012). The liquation cracking behavior of IN738LC superalloy during low power Nd:YAG pulsed laser welding. *Materials Characterization,* Vol.67, pp. 65–73.

[22] Mumtaz K.A., Erasenthiran P., Hopkinson N. (2008). High density selective laser melting of Waspaloy®. *Journal of Materials Processing Technology,* Vol. 195 (2008), pp. 77–87.

[23] Mumtaz K., Hopkinson N. (2009). Top surface and side roughness of Inconel 625 parts processed using selective laser melting. *Rapid Prototyping Journal*, Vol. 15/2, pp. 96–103.

[24] Murr L.E., Martinez E., Amato K.N., Gaytan S.M., Hernandez J., Ramirez D.A., Shindo P.W., Medina F., Wicker R.B. (2012). Metal fabrication by additive manufacturing using laser and electron beam melting technologies. *Journal of Materials Science and Technology,* Vol. 28(1), pp. 1–14.

[25] Nazarov A., Safronov V., Khmyrov R., Shishkovsky I. (2015). Fabrication of gradient structures in the Ni–Al system via SLM process. *IUTAM Symposium on Growing Solids*, June 23–27, Moscow, Russia.

[26] Nie P., Ojo O.A., Li Z. (2014). Numerical modeling of microstructure evolution during laser additive manufacturing of a nickel-based superalloy. *Acta Materialia,* Vol. 77, pp. 85–95.

[27] Ocylok S., Weisheit A., Kelbassa I. (2010) Functionally graded multi-layers by laser cladding for increased wear and corrosion protection, *Physics Procedia* Vol. 5, pp. 359–367.

[28] Oh J.H., Kirihara S., Miyamoto Y., Matsuura K., Kudoh M. (2002). Process control of reactive rapid prototyping for nickel aluminides. *Materials Science and Engineering A,* Vo. 334, pp. 120–126.

[29] Pang M., Yu G., Wang H.-H., Zheng C.-Y. (2008). Microstructure study of laser welding cast nickel-based superalloy K418. *Journal of Materials Processing Technology,* Vol. 207, pp. 271–275.

[30] Paul C.P., Mishra S.K., Premsingh C.H., Bhargava P., Tiwari P., Kukreja L. M. (2012). Studies on laser rapid manufacturing of cross-thin-walled porous structures of In-

conel 625. *International Journal of Advanced Manufacturing Technology,* Vol. 61, pp.757–770.

[31] Qin L., Hu J., Cui C., Wang H., Guo Z. (2008). Effect of al content on reaction laser sintering of Ni–Al powder. *Science of Sintering,* Vol. 40, pp. 295–301.

[32] Qin L., Hu J., Cui C., Wang H., Guo Z. (2009). Effect of Al content on reaction laser sintering of Ni–Al powder. *Journal of Alloys and Compounds,* Vol. 473, pp. 227–230.

[33] Ren X.D., Zhan Q.B., Yuan S.Q., Zhou J.Z., Wang Y., Ren N.F., Sun G.F., Zheng L.M., Dai F.Z., Yang H.M., Dai W.J. (2014). A finite element analysis of thermal relaxation of residual stress in laser shock processing Ni-based alloy GH4169. *Materials and Design,* Vol. 54, pp. 708–711.

[34] Safdar S., Pinkerton A.J., Li L., Sheikh M.A., Withers P.J. (2013). An anisotropic enhanced thermal conductivity approach for modeling laser melt pools for Ni-base super alloys. *Applied Mathematical Modelling,* Vol. 37, pp. 1187–1195.

[35] Shishkovsky I.V., Makarenko A.G., Petrov A.L. (1999). Conditions for SHS of intermetallic compounds with selective laser sintering of powdered compositions. *Combustion, Explosion, and Shock Waves,* Vol. 35 (2), pp. 166–170. doi: 10.1007/BF02674431.

[36] Shishkovsky I.V. (2001) Synthesis of functional gradient parts via RP methods. *Rapid Prototyping Journal,* Vol. 7, N 4, pp. 207–211. doi: 10.1108/13552540110402908.

[37] Shishkovsky I.V., Kuznetsov M.V., Morozov Yu.G. and Parkin I.P. (2004) Laser-induced combustion synthesis of 3D functional materials: computer-aided design. *Journal of Materials Chemistry.* Vol. 14, pp. 3444–3448. doi: 10.1039/b406732k.

[38] Shishkovsky I., Missemer F., Smurov I. (2012). Direct metal deposition of functional graded structures in Ti-Al system. *Physics Procedia.* Vol. 39, pp. 382–391. doi: 10.1016/j.phpro.2012.10.052

[39] Shishkovsky I., Missemer F., Kakovkina N., Smurov I. (2013a). Intermetallics synthesis in the Fe–Al system via layer-by layer 3D laser cladding. *Crystals.* Vol. 3, pp. 517–529. doi:10.3390/cryst3040517.

[40] Shishkovsky I., Yadroitsev I., Smurov I. (2013b) Fabrication of 3D parts from titanium nickel via layerwise selective laser melting. *Technical Physics Letters.* Vol. 39(12), pp. 1081–1084. doi: 10.1134/S1063785013120250

[41] Shishkovsky I.V. (2015) Laser controlled intermetallics synthesis during surface cladding. In: J. Lawrence et al. (Eds.), *Laser Surface Engineering. Processes and Applications,"* pp. 237–286. Woodhead Publishing Series in Electronic and Optical Materials, Elsevier Science and Technology, on-line ISBN 978-1-78242-074-3.

[42] Sims C.T., Stoloff N.S., Hagel W.C. (1995). *Superalloys.* Part I–II. John Willey & Sons Publ. 384 p.

[43] Song B., Dong S., Coddet P., Liao H., Coddet C. (2014) Fabrication of NiCr alloy parts by selective laser melting: columnar microstructure and anisotropic mechanical behavior. *Materials and Design,* Vol. 53, pp. 1–7.

[44] Theriault, Xue L., Dryden J.R. (2009). Fatigue behavior of laser consolidated IN-625 at room and elevated temperatures. *Materials Science and Engineering A,* Vol. 516, pp. 217–225.

[45] Verdi D., Garrido M.A., Munez C.J., Poza P. (2015). Cr3C2 incorporation into an Inconel 625 laser cladded coating: effects on matrix microstructure, mechanical properties and local scratch resistance. *Materials and Design,* Vol. 67, pp. 20–27.

[46] Vilar R., Santos E.C., Ferreira P.N. (2009). Structure of NiCrAlY coatings deposited on single-crystal alloy turbine blade material by laser cladding. *Acta Materialia,* Vol. 57(18), pp. 5292–5302.

[47] Wang GH., Zuo D., Sun Y., Xu F., Zhang D. (2009). Microstructure of nanometer Al2O3 dispersion strengthened Ni-based high-temperature protective coatings by laser cladding. *Transactions of Nonferrous Metals Society of China*, Vol. 19, pp. 586–591.

[48] Wang H., Zuo D., Li X., Chen K., Huang M. (2010a). Effects of CeO2 nanoparticles on microstructure and properties of laser cladded NiCoCrAlY coatings. *Journal of Rare Earths,* Vol. 28(2), Apr., p. 246.

[49] Wang H., Zuo D., Chen G., Sun G., Li X., Cheng X. (2010b). Hot corrosion behaviour of low Al NiCoCrAlY cladded coatings reinforced by nano-particles on a Ni-base super alloy. *Corrosion Science,* Vol. 52, pp. 3561–3567.

[50] Wang H., Zuo D., Wang M., Sun G., Miao H., Sun Y. (2011). High temperature frictional wear behaviors of nano-particle reinforced NiCoCrAlY cladded coatings. *Transactions of Nonferrous Metals Society of China,* Vol. 21, pp. 1322–1328.

[51] Yuan Y., Gu Y.F., Zhong Z.H., Shi Z., Osada T., Yokokawa T., Harada H. (2013). γ precipitation in the primary γ' of a new Ni–Co-base disc superalloy. *Materials Science and Engineering A,* Vol. 579, pp. 35–40.

[52] Yu, Y., Zhou, J., Chen J. (2012). Preparation, microstructure and tribological behavior of laser cladding NiAl intermetallic compound coatings, *Wear,* Vol. 274– 275, pp. 298–305.

[53] Zakiev S.E., Kholpanov L.P., Parkin I.P., Kuznetsov M.V., Morozov Yu. G., Shishkovskii I.V. (2006) Modeling of the thermal processes that occur in the laser sintering of reacting powder compositions. *Applied Physics A,* Vol. 84(1–2), July, pp. 123–129. doi: 10.1007/s00339-006-3586-0.

[54] Zhang G.Q., Yao J., Mazumder J. (2011). Laser direct metal deposition technology and microstructure and composition segregation of Inconel 718 Superalloy. *Journal of Iron and Steel Research, International,* Vol.18(4), pp. 73–78.

[55] Zhang C., Li L., Deceuster A. (2011). Thermomechanical analysis of multi-bead pulsed laser powder deposition of a nickel-based superalloy. *Journal of Materials Processing Technology,* Vol. 211, pp. 1478–1487.

[56] Zhang Y.N., Cao X., Wanjara P., Medraj M. (2013). Oxide films in laser additive manufactured Inconel 718. *Acta Materialia,* Vol. 61, pp. 6562–6576.

[57] Zhao J., Cao W., Ge C., Tan Y., Zhang Y., Fei Q. (2009a). Research on laser engineered net shaping of thick-wall nickel-based alloy parts. *Rapid Prototyping Journal,* Vol. 15/1, pp. 24–28.

[58] Zhao X., Lin X., Chen J., Xue L., Huang W. (2009b). The effect of hot isostatic pressing on crack healing, microstructure, mechanical properties of Rene88DT superalloy prepared by laser solid forming. *Materials Science and Engineering A,* Vol. 504, pp. 129–134.

[59] Zhong M., Sun H., Liu W., Zhu X., He J. (2005). Boundary liquation and interface cracking characterization in laser deposition of Inconel 738 on directionally solidified Ni-based superalloy. *Scripta Materialia,* Vol. 53, pp. 159–164.

[60] Zhou S., Dai X., Zheng H. (2011). Analytical modeling and experimental investigation of laser induction hybrid rapid cladding for Ni-based WC composite coatings. *Optics and Laser Technology,* Vol. 43, pp. 613–621.

[61] Zhou S., Xiong Z., Dai X., Liu J., Zhang T., Wang C. (2014). Microstructure and oxidation resistance of cryomilled NiCrAlY coating by laser induction hybrid rapid cladding. Surface and Coatings Technology, Vol. 258, pp. 943–949.

IntechOpen